DOI: 10.1002/chem.200700375

One-Step Synthesis of Highly Water-Soluble Magnetite Colloidal Nanocrystals

Jianping Ge,[a] Yongxing Hu,[a] Maurizio Biasini,[b] Chungli Dong,[c] Jinghua Guo,[c] Ward P. Beyermann,[b] and Yadong Yin*[a]

Abstract: A high-temperature solution-phase hydrolysis approach has been developed for the synthesis of colloidal magnetite nanocrystals with well-controlled size and size distribution, high crystallinity, and high water solubility. The synthesis was accomplished by the hydrolysis and reduction of iron(III) cations in diethylene glycol with a rapidly injected solution of sodium hydroxide at an elevated temperature. The high reaction temperature allows for control over size and size distribution and yields highly crystalline products. The superior water solubility is achieved by using a polyelectrolyte, that is, poly(acrylic acid) as the capping agent, the carboxylate groups of which partially bind to the nanocrystal surface and partially extend into the surrounding water. The direct synthesis of water-soluble nanocrystals eliminates the need for additional surface modification steps which are usually required for treating hydrophobic nanocrystals produced in nonpolar solvents through the widely recognized pyrolysis route. The abundant carboxylate groups on the nanocrystal surface allow further modifications, such as bioconjugation, as demonstrated by linking cysteamine to the particle surface. The monodisperse, highly water-soluble, superparamagnetic, and biocompatible magnetite nanocrystals should find immediate important biomedical applications.

Keywords: hydrolysis · magnetite · nanostructures · superparamagnetic properties · water

Introduction

The major impetus in developing well-defined superparamagnetic nanocrystals has been their biomedical applications as they are not subject to strong magnetic interactions in dispersion.[1,2] Iron oxide nanocrystals have received the most attention for this purpose because of their biocompatibility and stability in physiological conditions.[3–7] Several robust solution-phase approaches have been developed for synthesizing magnetic iron oxide (e.g. γ-Fe_2O_3 or Fe_3O_4) nanoparticles with high crystallinity and tightly controlled size and monodispersity, typically through organometallic pyrolysis reactions or solvothermal processes at elevated temperatures in nonpolar organic solvents.[8–14] Additional steps for surface modification or lipid encapsulation are usually required to transfer the hydrophobic products from nonpolar solvents to water, and make them active for biomedical applications.[15–17] Besides the practical difficulties in phase transfer, the stability of these dispersions has been another major concern in these approaches.[18] Iron oxide particles have also been prepared directly in water or reversed micelles by precipitating Fe^{2+} and Fe^{3+} cations, typically with a lower degree of control over the size, distribution and crystallinity because of the low reaction temperature.[19–21]

To produce high quality water-soluble nanocrystals, we found it necessary to take advantage of concepts developed previously for the pyrolytic growth of hydrophobic colloidal nanocrystals in nonpolar organic solvents. A high reaction temperature is required to directly synthesize water-soluble nanocrystals with high crystallinity and narrow size distribution control, which can be achieved by using solvents such as polyhydric alcohols. The challenge is to then find an appropriate capping agent, which is thermally stable at increased reaction temperatures and able to maintain hydrophilicity after binding to electron-poor iron atoms at the

[a] Dr. J. Ge, Y. Hu, Prof. Y. Yin
Department of Chemistry, University of California
Riverside, CA 92521 (USA)
Fax: (+1) 951-827-4713
E-mail: yadong.yin@ucr.edu

[b] Dr. M. Biasini, Prof. W. P. Beyermann
Department of Physics and Astronomy, University of California
Riverside, CA 92521 (USA)

[c] Dr. C. Dong, Dr. J. Guo
Advanced Light Source, Lawrence Berkeley National Laboratory
Berkeley, CA 94720 (USA)

Supporting information for this article is available on the WWW under http://www.chemeurj.org/ or from the author.

nanocrystal surface. Typically used small organic surfactants are not useful for this purpose as either they are unstable at high temperatures or they precipitate the particles out of the polar solvent after binding to the particle surface. We find that short-chain poly(acrylic acid) (PAA) is an ideal candidate as a capping agent for such reactions. Here, we demonstrate its use in a one-step process for synthesizing highly water-soluble magnetite (Fe_3O_4) nanocrystals with uniform sizes. Specifically, superparamagnetic Fe_3O_4 nanocrystals were produced by hydrolyzing the iron precursor $FeCl_3$ with a NaOH solution at a temperature above 200 °C in diethylene glycol (DEG, boiling point ≈244–245 °C) in the presence of PAA. As schematically illustrated in Figure 1, the carboxylate groups on the PAA chains strongly

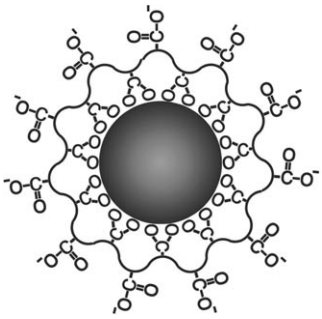

Figure 1. Schematic illustration of PAA-capped Fe_3O_4 nanocrystals. A fraction of carboxylate groups bind to nanocrystal surfaces and the remaining fraction extend into the surrounding water, rendering the nanocrystals highly soluble in water.

coordinate to iron cations on the magnetite surface to form a robust coating, while uncoordinated carboxylate groups extend into the aqueous solution, conferring upon the particles a high degree of dispersibility in water. The large number of uncoordinated carboxylate groups on the nanocrystal surface can be used for further linkage of biomolecules through the well-developed bioconjugation chemistry. The superparamagnetism, small and uniform particle size, and biocompatibility make these magnetite nanocrystals ideal for a number of biomedical applications, such as highly sensitive magnetic biolabeling, efficient bioseparation, and contrast enhancement for magnetic resonance imaging (MRI). The iron source used in this approach is commercially available, inexpensive, and more environmentally acceptable than iron pentacarbonyl, $Fe(CO)_5$, a highly toxic precursor commonly used in thermal decomposition routes. Therefore, this approach follows the green chemistry principle by providing an environmentally and economically preferable alternative for preparing high-quality magnetite nanocrystals.

Results and Discussion

Size control and phase determination: The high-temperature hydrolysis of Fe^{3+} upon addition of NaOH in the presence of PAA yields highly water-soluble and uniform magnetite nanocrystals, as shown in the TEM images in Figure 2. The hydrolysis of Fe^{3+} is initiated by the production of water

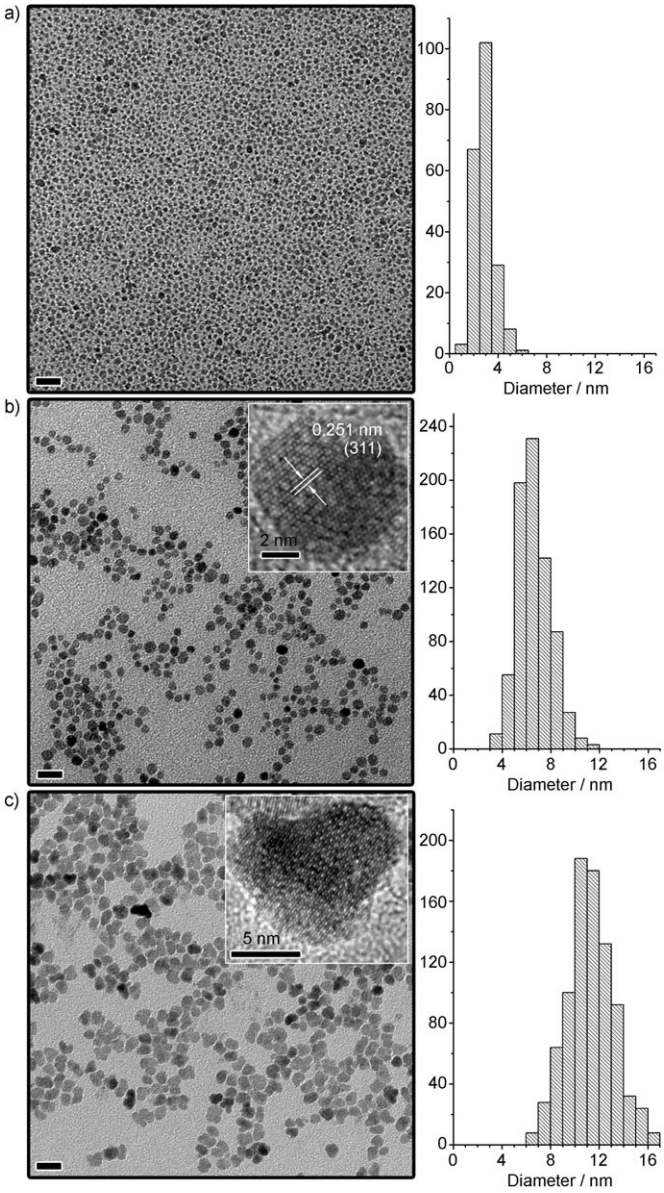

Figure 2. Representative TEM images and the corresponding measured size distributions of Fe_3O_4 nanocrystals with an average diameter of a) 2.9 nm, b) 6.6 nm, and c) 11.3 nm, respectively. The size of the nanocrystals is controlled by changing the amount of NaOH or the reaction time. All the scale bars are 20 nm. Insets are HRTEM images of individual nanocrystals in Figure 2b and c, showing the single crystalline structures.

through the neutralization reaction between NaOH and PAA. The increased alkalinity upon addition of NaOH also favors the hydrolysis reaction. Under the reductive atmosphere provided by DEG at high temperature,[22,23] $Fe(OH)_3$ partially transforms to $Fe(OH)_2$, finally leading to the for-

mation of Fe_3O_4 particles through dehydration. The size of the nanocrystals can be precisely controlled by simply changing the amount of NaOH added while keeping all other parameters fixed, as shown in the two examples in Figure 2a and b. This size tunability might be the result of slight differences in H_2O concentration and alkalinity caused by varying NaOH concentrations. When NaOH is sufficient, the amount of H_2O and the alkalinity is enough to fully hydrolyze the Fe^{3+} so that both the nucleation and growth can be relatively quick. When the amount of NaOH is low, the growth of nanocrystals is much slower due to the low alkalinity and limited supply of H_2O. When the samples were collected at about the same time after the initiation of reaction, the nanocrystals produced with less NaOH was smaller due to a much lower growth rate. Therefore, the increased amount of NaOH results in higher H_2O concentration and relatively stronger alkalinity, promoting the formation of larger oxide nanocrystals.

The growth of magnetite nanocrystals follows the classic La Mer model, in which monodisperse particles are favored by a temporally discrete nucleation event followed by slower controlled growth on the existing nuclei.[24,25] Thanks to the high reaction temperature, a relatively rapid nucleation occurs shortly after the injection of NaOH, leading to magnetite nanocrystals with narrow size distributions (Figure 2b).[26] Interestingly, further heating of the system for an additional one hour does not significantly broaden the size distribution of nanocrystals, which occurs in many other synthetic systems, suggesting relatively slow particle growth in the current system. During this period, the remaining precursors are continuously consumed and added to existing particles. Further growth of nanocrystals is dominated by the well-known Ostwald ripening process in which small nanocrystals dissolve as a result of their high surface energy and the material is subsequently redeposited on the larger nanocrystals.[25] Figure 2c shows the nanocrystals obtained after heating the same system in Figure 2b for an additional 24 h. We have determined the diameter of large irregular-shaped particles by measuring their longest dimensions. The average diameter increases significantly from 6.6 ± 1.36 to 11.3 ± 1.88 nm while the relative size distribution narrows slightly, suggesting the ripening mechanism during the growth. By controlling the reaction conditions, such as the amount of NaOH and the reaction time, we have been able to conveniently tune the average size of the nanocrystals from $\approx$2 to $\approx$15 nm.

High-temperature annealing during synthesis yields highly crystalline magnetite particles. Inspections of the products by using HRTEM indicates that each particle is a well-ordered single crystal, as shown in the inset of Figure 2b. Measuring the distance between two adjacent lattice fringes gives a value of 0.251 nm, which corresponds to the lattice spacing of (311) planes of cubic magnetite. We have also inspected the large irregular-shaped nanoparticles produced after 24 h annealing. As shown in the inset of Figure 2c, the particles are still single crystals without defects. This observation again confirms the ripening growth mechanism and rules out the possible fusion mechanism in which defects such as twins should be easily observed in the final products.

The crystal structure of the products was also studied by measuring their XRD patterns. Figure 3 shows the diffraction patterns with apparent broadenings for 2.9 and 6.6 nm nanocrystals, which could be indexed to a cubic-phase Fe_3O_4. The Debye–Scherrer formula $D_{hkl}=k\lambda/\beta cos\theta$ was used to estimate an average crystallite size from the XRD patterns, in which D_{hkl} is the particle size parallel to the (hkl) plane, k is a geometrical constant with a typical value of 0.89 for spherical particles, λ is the wavelength of the radiation, β is the full width at half maximum (FWHM) in radians, and θ is the position of the diffraction peak. Calculations using the strongest peaks (311) give grain sizes of 3.6 and 6.4 nm respectively, which are comparable to the TEM statistical results.

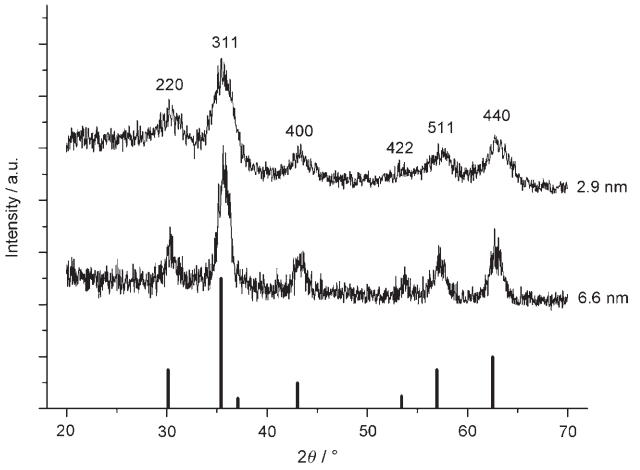

Figure 3. X-ray powder diffraction pattern for 2.9 and 6.6 nm Fe_3O_4 nanocrystals. Peak positions and relative intensities recorded in the literature for bulk Fe_3O_4 samples are indicated by the vertical bars.

As magnetite (Fe_3O_4) and maghemite (γ-Fe_2O_3) have very similar XRD patterns and both of them show magnetic behavior, XAS spectroscopy was used to definitively identify the crystal phase and composition of the products. Figure 4 shows the Fe L-edge X-ray absorption of the as-prepared samples. For Fe L-edge X-ray absorption, the splitting of the L_3 peak located at 705–710 eV and the ratio of two L_2 peaks at 719–725 eV are two important features for distinguishing between Fe_3O_4, γ-Fe_2O_3, and α-Fe_2O_3. The splitting of peaks A and B in Figure 4 was measured to be 1.12 eV, which is close to the value reported in the literature for Fe_3O_4 (1.2 eV for Fe_3O_4, 1.4 eV for γ-Fe_2O_3, 1.6 eV for α-Fe_2O_3).[27] The relatively stronger peak at C in comparison to the peak at D for the L_2 edge also supports the conclusion that the nanocrystals are Fe_3O_4 in composition.[28]

Surface chemistry and high water solubility: Two factors contribute to the robust surface coating of PAA on the magnetite nanocrystals: the strong coordination of carboxylate groups with surface iron cations and the multiple anchor

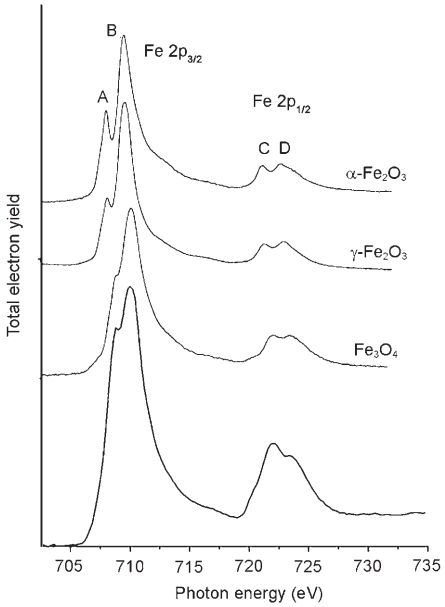

Figure 4. XAS spectrum at Fe L-edge of 6.6 nm Fe_3O_4 nanocrystals and referential spectra for Fe_3O_4, γ-Fe_2O_3, α-Fe_2O_3 .[27]

points for every single polymer chain. The stability of the PAA coating on magnetite nanocrystal surfaces was demonstrated by measuring the FTIR spectrum on a sample that was cleaned three times by repeated actions of precipitation with ethanol and redispersion in water and finally dried in a powdered form. The three peaks shown in Figure 5b and located at 1454, 1566, and 1406 cm^{-1} can be attributed to characteristic bands of the carboxylate (COO^-) groups, corresponding, respectively, to the CH_2 bending mode, asymmetric and symmetric C–O stretching modes of the COO^- group.[29,30] For comparison, Figure 5a shows the FTIR spectrum of pure PAA, which indicates a strong absorption band at $\approx$1718 cm^{-1}. This band is characteristic of the C=O stretching mode for protonated carboxylate groups, which form cyclic dimers and sideways chains due to hydrogen bonding. By comparing these spectra, it is clear that a large amount of carboxylate groups remain on the surface of nanocrystals even after extensive washing.

The uncoordinated carboxylate groups on the polymer chains extend into the aqueous solution, conferring upon the particles a high degree of dispersibility in water. These uncoordinated carboxylate groups can also be protonated by adding HCl to the nanocrystal solution. At a pH $\approx$4, the nanocrystals start to aggregate and precipitate out from the solution, as will be discussed in detail later. The FTIR spectrum of such a precipitate is shown in Figure 5c. Similar to that of pure PAA, a strong peak around $\approx$1716 cm^{-1} appears due to the C=O stretching mode for protonated carboxylate groups. In addition to the three characteristic bands from carboxylate groups, a new band is distinguishable at 1626 cm^{-1} which appears as a shoulder before protonation (Figure 5b) and can be attributed to the C–O stretching mode of partial carboxylate groups.[29]

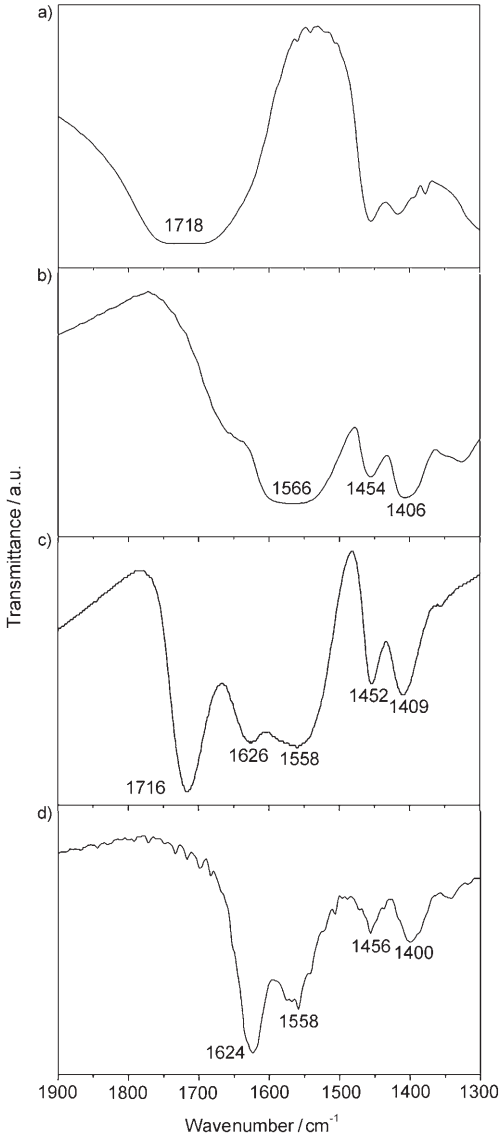

Figure 5. FTIR spectrum of a) pure PAA, b) PAA carboxylate-capped Fe_3O_4 nanocrystals, c) PAA carboxyl-capped Fe_3O_4 nanocrystals, and d) Fe_3O_4 nanocrystals conjugated to cysteamine.

The strong surface binding of PAA confers upon the magnetite nanocrystals high solubility in water and in many buffer solutions, such as phosphate-buffered saline (PBS). The as-synthesized nanocrystals, after washing with ethanol and water three times, can be precipitated and collected by centrifugation or magnetic force, and finally form a dry powder after heating at 60 °C for 2 h, as shown in Figure 6b. This powder can be readily redispersed in water to form a stable solution within seconds. Due to their small size and superparamagnetic properties, these nanocrystals show ferrofluidic behavior when the solution is subjected to an external magnetic field, as shown in Figure 6d.

Figure 6c shows the relationship between the concentration of nanocrystals and the pH values of water solution. The nanocrystals are dispersible in water at a pH value

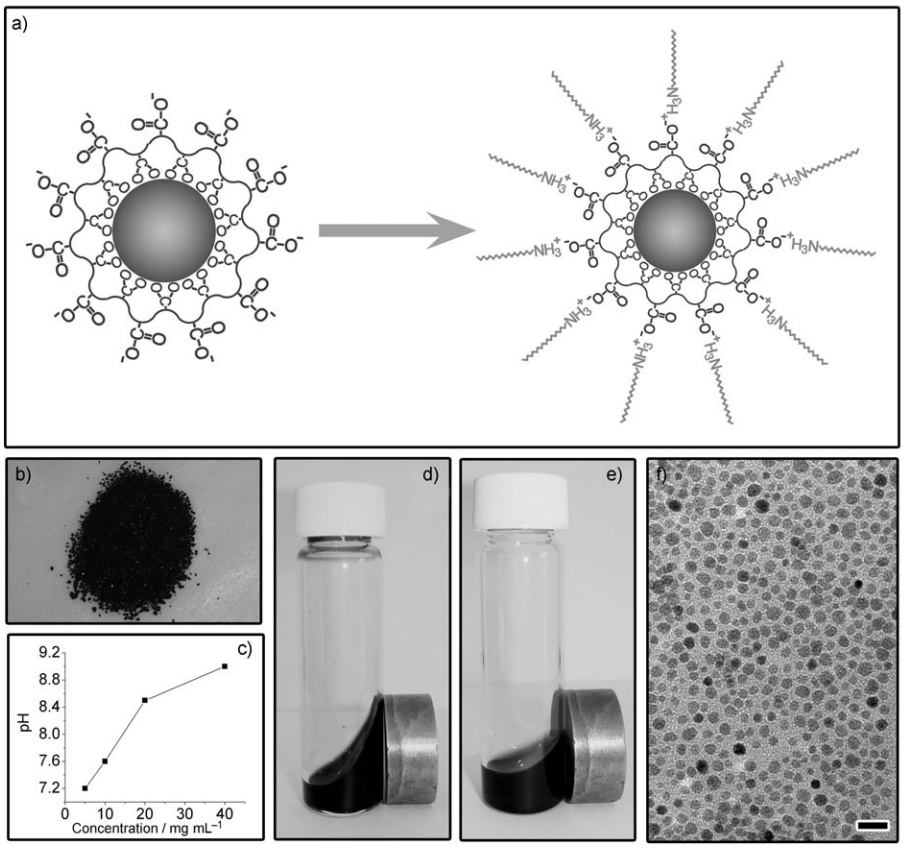

Figure 6. a) Schematic illustration of the hydrophilic–hydrophobic transition of the nanocrystals by complexing the surface carboxylate groups with oleylamine through the electrostatic interaction. b) Photo of the powder of Fe_3O_4 nanocrystals collected by precipitating the as-synthesized sample which was dried at 60 °C. c) pH value of the Fe_3O_4 aqueous solution as a function of concentration. d,e) Photos of Fe_3O_4 nanocrystal solutions in d) water and e) toluene in response to external magnetic fields. f) Typical TEM image of Fe_3O_4 nanocrystals dispersed in toluene.

above 4.0, and the solubility increases dramatically with the pH value as more carboxylate groups are ionized at higher pH. In the weak acid solution, the surface carboxylate groups are partially ionized so that the solubility of the nanocrystals decreases. At a pH value below 4.0, the nanocrystals are no longer stable in water and form aggregates which can be easily separated from the solution by using an external magnetic field. We believe that this is because most of the carboxylate groups assume the less hydrophilic protonated form at low pH and the hydrophobic backbone of PAA chains dominates the solubility. The instability of the nanocrystals at low pH provides another effective way (in addition to ethanol precipitation) for their separation from the solution; the precipitates can then be conveniently extracted from the solution by using an external magnetic field.

Phase transfer to nonpolar solvent: The abundant carboxylate groups on the surface of magnetite nanocrystals provide the opportunity for further surface modification, through either the electrostatic interaction or chemical bonding. Here we first demonstrate that the hydrophilic surface can be easily converted to a hydrophobic one by attaching oleylamine molecules to the PAA coated nanocrystals through the electrostatic interaction between carboxylate and ammonium groups (Figure 6). The as-synthesized Fe_3O_4 nanocrystals were separated from water by adding hydrochloric acid to the solution, and at the same time surface COO^- groups are protonized to COOH. Then oleylamine was linked to the nanocrystals through neutralization and subsequent electrostatic interaction, which induce the reversal of the polarity and make the nanocrystals very soluble in a nonpolar solvent such as toluene.[31] Similar to a water solution of the PAA coated nanocrystals, the toluene solution of surface-modified nanocrystals is stable over months, and shows ferrofluidic behavior under an external magnetic field (Figure 6e). The nanocrystals commonly self-assemble into a monolayer on the carbon substrate of a TEM grid without the formation of aggregates, confirming the success of phase transfer (Figure 6f).

Bioconjugation: The key advantage of the PAA-caped nanocrystals also lies in their convenient conjugation to biological molecules by using an appropriate bifunctional linker and any one of the well-established techniques.[32] Here, we simply demonstrate the feasibility of this approach by linking cysteamine molecules to the nanocrystal surface through conjugation with 1-ethyl-3-(3-dimethylaminopropyl)carbodiimide hydrochloride (EDC, Figure 7). As-synthesized Fe_3O_4 nanocrystals were separated from water by addition of hydrochloric acid, and cysteamine was conjugated to the nanocrystals by using the carbodiimide cross-linker. The corresponding FTIR spectrum of the conjugated nanocrystals (Figure 5d) shows two peaks around 1624 and 1558 cm^{-1}, which are commonly ascribed to amide I (C=O stretching vibration of amide) and amide II (N–H bending vibration of the secondary amide).[33,34] The thiol-functionalized magnetic nanocrystals can be further attached to surfaces of gold colloids by the strong covalent Au–S bond, producing composite nanostructures as shown in Figure 7d–f. Originally, the gold colloids are stabilized in water by the citrate ions. We noticed that even trace amounts of cysteamine would substitute the citrate ions and cause the aggregation of gold parti-

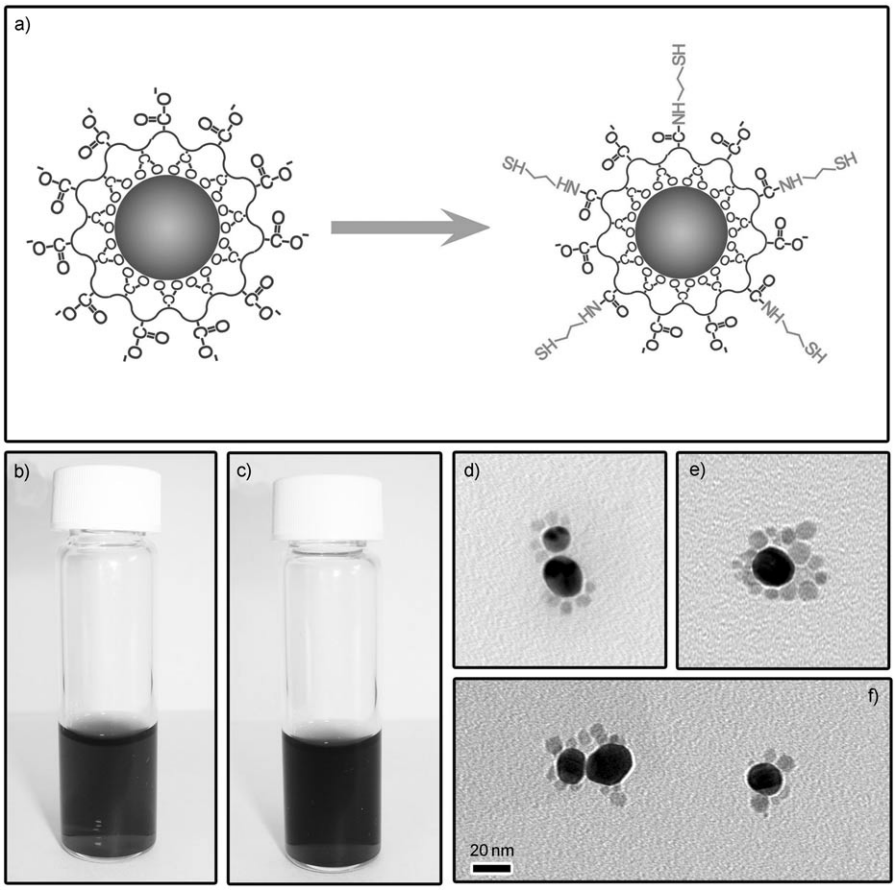

Figure 7. a) Schematic illustration of linking cysteamine molecules to a Fe_3O_4 nanocrystal surface through the EDC conjugation by forming amide bonds. b,c) Photos of b) Au colloids stabilized by citrate and c) Au colloids stabilized by cysteamine conjugated Fe_3O_4 nanocrystals. d–f) Representative TEM images of Au–Fe_3O_4 composite nanostructures.

cles. However, the diluted gold colloidal solution remains stable after the introduction of cysteamine-functionalized magnetite nanocrystals due to the stabilization provided by the unreacted carboxylate groups on the magnetite surface. The typical isolated Au–Fe_3O_4 composite nanostructures shown in Figure 7d–f also clearly indicate the presence of thiol groups on the magnetite surface. The successful conjugation of cysteamine to PAA-capped magnetite nanocrystals suggests the great potential for linking other biomolecules to the magnetite nanocrystals for applications such as magnetic biomedical labeling, targeted delivery, and magnetic resonance imaging.

Magnetic property measurements: The magnetic properties of the Fe_3O_4 nanocrystals, including hysteresis loops, remanence, coercivity, susceptibility, and blocking temperature, were systematically studied by using a SQUID magnetometer. Figure 8a and b show the magnetization of 6.6 nm Fe_3O_4 nanocrystals versus the applied field at 300 and 2 K by cycling the field between −20 to 20 kOe. As expected, the nanocrystals are superparamagnetic at room temperature, showing no remanence or coercivity. At 2 K, the thermal energy is insufficient to induce moment randomization so that the nanocrystals show typical ferromagnetic hysteresis loops with a remanence of 8.0 emu g^{-1} and a coercivity of 400 Oe. The saturated mass magnetization of the nanocrystals at 300 and 2 K is 19.5 and 25.6 emu g^{-1}, respectively. It is worth noting that the average mass contribution of the surfactant layer of these nanocrystals has been estimated to be 53% through thermogravimetric measurements. Therefore, the values of saturated mass magnetization of pure magnetite nanocrystals are expected to be much higher. For these small, superparamagnetic particles, the magnetic moment of a single nanocrystal, μ, may be estimated from the Langevin paramagnetic function: $M(x)=N\mu(\coth x-(1/x))$, in which $x=\mu H/k_BT$, N is the number of clusters, H is the applied field, k_B is the Boltzmann's constant, and T is the absolute temperature. Fitting the data in Figure 8a to this function, the magnetic moment for a 6.6 nm nanocrystal at room temperature is calculated to be $9.40\times10^3\mu_B$ (8.72×10^{-17} emu).

It is well known that below a critical size, each ferromagnetic nanocrystal can only support a single magnetic domain, and so can be viewed as a single large magnetic moment of roughly 10^3–$10^5\,\mu_B$. At low temperature, this moment points along the energetically favorable crystallographic axis, giving the particle a remanence on laboratory time scales. Above a certain temperature, the thermal fluctuations overcome the anisotropy barrier and randomize the magnetic moment so that the net moment is zero, leading to superparamagnetic behaviors of the nanocrystals. This temperature, called the blocking temperature, is an important feature of the superparamagnetic nanocrystals. Figure 9a and b show the temperature dependence of magnetic susceptibility and remanence for the 6.6 nm Fe_3O_4 nanocrystals. A maximum susceptibility of 0.046 emu $Oe^{-1}g^{-1}$ is observed for the zero-field-cooled (ZFC) curve, which is located at 100 K. As ZFC and FC scans overlap at temperatures at which the sample is in thermal equilibrium, the lowest temperature for which this occurs, that is, cases where the ZFC susceptibility is a maximum, is commonly considered the blocking temperature of the magnetic nanocrystals. The

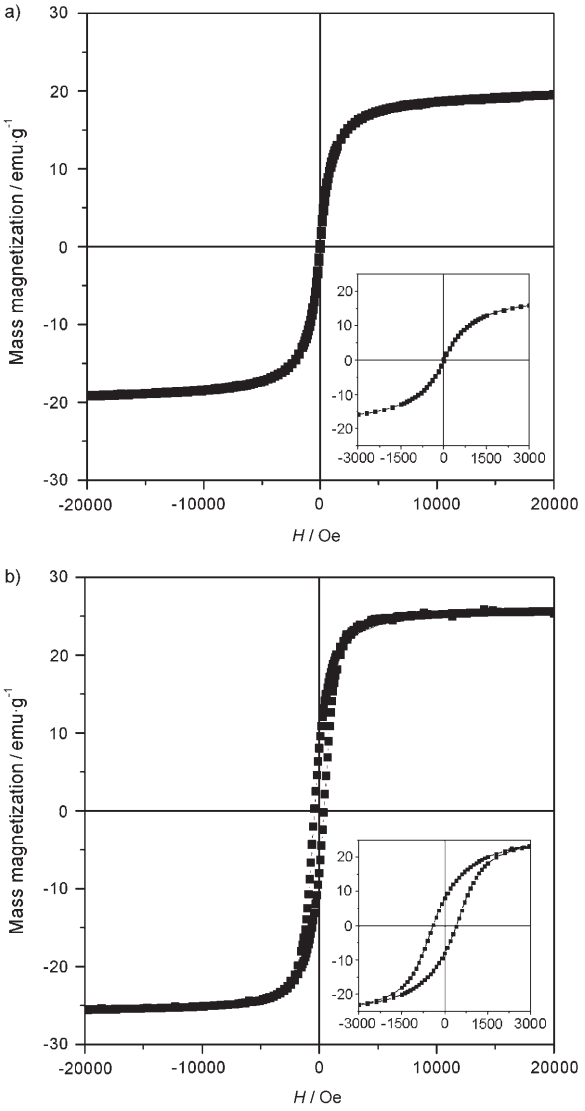

Figure 8. Magnetization as a function of field for 6.6 nm diameter Fe_3O_4 nanocrystals at a temperature of a) 300 K and b) 2 K. Insets show the data around zero field with an expanded scale ranging from −3000 to 3000 Oe.

presence of a remanent signal below 100 K demonstrates the gradual blocking of the moments below this temperature, which is in good agreement with the susceptibility results.

The temperature dependence of magnetization is also an important property for both fundamental studies and technical applications. In general, the spontaneous magnetization $M(T)$ far below the Curie temperature should follow the Bloch law: $M(T)=M(0)(1\text{-}BT^b)$, for which $M(0)$ is the magnetization at 0 K, B is the Bloch constant, and b is the Bloch exponent. The Bloch exponent b has been verified to be 1.5 for bulk materials. Figure 10 shows the saturation magnetization as a function of temperature in a field of 6 T for the synthesized Fe_3O_4 nanocrystals. Fitting the data to the Bloch law, the Bloch constant is found to be 9.17×10^{-6} and the

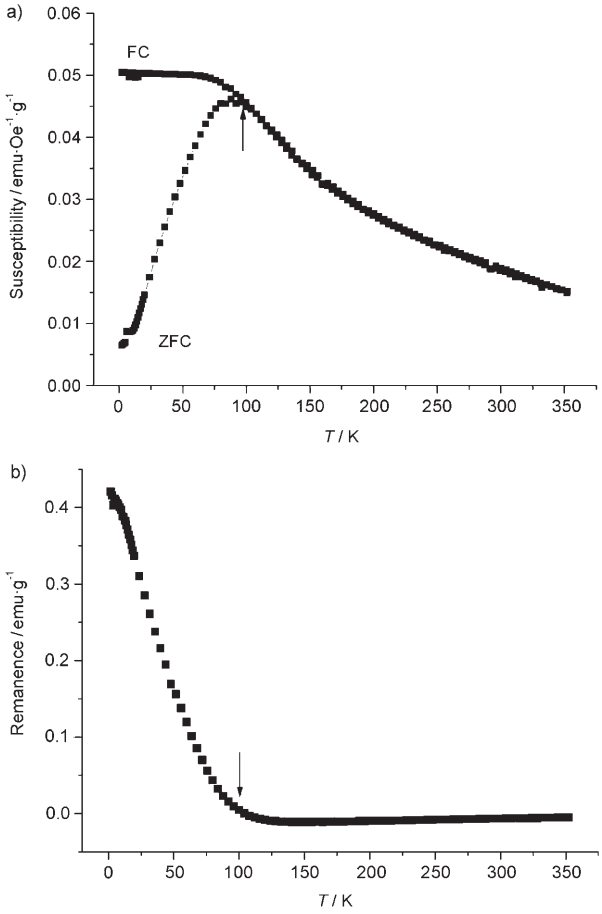

Figure 9. a) Low-field susceptibility as a function of temperature measured after zero-field cooled and field cooled in a 10 Oe field. b) Remanence as a function of temperature after a 6 T external magnetic field was removed.

Bloch exponent is 1.7, which agree well with the results from theoretical calculations and experimental measurements.[35,36]

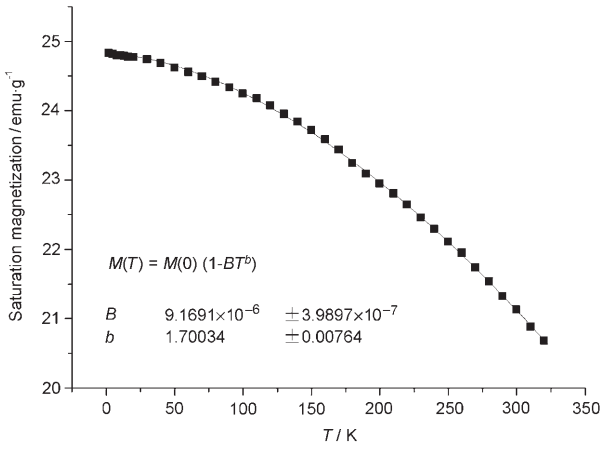

Figure 10. Saturation magnetization data (■) as a function of temperature, measured with a field of 6 T for Fe_3O_4 nanocrystals with an average size of 6.6 nm. ——: A fit to the data by the Bloch law.

Conclusion

We have successfully developed a high-temperature solution-phase hydrolysis procedure for the synthesis of colloidal magnetite nanocrystals with well-controlled size and size distribution, high crystallinity and high water solubility. Unlike the widely recognized pyrolysis route which produces hydrophobic nanocrystals in nonpolar organic solvent, we use a high boiling point polar solvent, DEG, as the reaction media so that the reaction can occur at an elevated temperature which benefits the precise control of the size and size distribution of the products. The high reaction temperature also allows sufficient rearrangement of atoms within a growing nanocrystal over the course of the synthesis, yielding highly crystalline products. The high water solubility is achieved by using a polyelectrolyte PAA as the capping agent, the carboxylate groups of which partially bind to the nanocrystal surface and partially extend into the surrounding water. The monodisperse, biocompatible, and superparamagnetic Fe_3O_4 nanocrystals can be conveniently synthesized in one step and they should easily find immediate important biomedical applications. We also expect that the concept of using the combination of high-boiling-point polar solvent, polyelectrolyte surfactant, and high-temperature reaction could be extended to the synthesis of water-soluble nanocrystals of a variety of other materials, the syntheses of which have been mostly limited in nonpolar organic solvents.

Experimental Section

Chemicals: Diethylene glycol (reagent grade), ethyl alcohol (denatured), hydrochloric acid (36.5–38%), toluene (99.8%), and sodium hydroxide (98.8%) were purchased from Fisher Scientific. Anhydrous iron(III) chloride (98%) was purchased from Riedel-de Haën. Poly(acrylic acid) ($M_w = 1{,}800$), oleylamine (70%), and cysteamine (95%) were obtained from Sigma-Aldrich. 1-Ethyl-3-(3-dimethylaminopropyl) carbodiimide hydrochloride (EDC) and *N*-hydroxysuccinimide (NHS) were purchased from PIERCE. All chemicals were directly used as received without further treatment.

Synthesis of water-soluble magnetite colloidal nanocrystals: The magnetite nanocrystals were synthesized by using a solution-phase hydrolysis reaction at a high temperature. A NaOH/DEG stock solution was prepared by dissolving NaOH (50 mmol) in DEG (20 mL); this solution was heated at 120 °C for 1 h under nitrogen, and cooled down and kept at 70 °C. In a typical synthesis, a mixture of PAA (4 mmol), $FeCl_3$ (2 mmol), and DEG (15 mL) were heated to ≈220 °C in a nitrogen atmosphere for 30 min under vigorous stirring, forming a transparent light-yellow solution. A NaOH/DEG stock solution (4 mL) was injected rapidly into the above hot mixture, which induced the temperature drop to ≈210 °C and the reaction solution turned black immediately. The resulting mixture was further heated for 10 min to yield magnetite nanocrystals with an average diameter of 6.6 nm. The size of nanocrystals can be tuned by controlling either the reaction time or the amount of NaOH solution. For example, heating the above solution continuously for 24 h leads to much larger nanocrystals (≈11.3 nm). The addition of less NaOH produces nanocrystals of smaller size, that is, 2.9 nm for 2 mL NaOH/DEG stock solution. The final products were washed by repeated actions of precipitation with ethanol and subsequent redispersion in deionized (DI) water several times, and finally redispersed in DI water (20 mL).

Phase transfer of magnetite colloidal nanocrystals: A diluted HCl solution was added to the above magnetite nanocrystal solution (5 mL) so that its pH value became ≈4.0. The nanocrystals precipitated instantly, which were subsequently separated from the solution by applying an external magnetic field. The nanocrystals were washed with anhydrous ethanol several times and collected by an external magnetic field. Finally, the precipitates were transferred to toluene (5 mL), in which the nanocrystals still remained insoluble. An addition of oleylamine (10 μL) to the mixture solubilises the nanocrystals instantly by complexing with surface carboxyl groups and forming hydrophobic surfaces.

Surface conjugation of magnetite nanocrystals: As-synthesized magnetite nanocrystals in aqueous solution (1 mL) were separated by the acid-precipitation method, washed with DI water three times, and suspended in water (10 mL). Cysteamine (192 μL), EDC (500 μL), and NHS (50 μL) were sequentially added to the solution, which was stirred at room temperature for 3 h. The thiol-grafted magnetite nanocrystals were washed by the acid-precipitation method to remove the excess cysteamine residues and then dispersed in water (5 mL, 6.7 $\mu mol\,mL^{-1}$, pH 6.4).

Gold colloids were prepared by the sodium citrate method, and the final concentration was 1.5 $\mu mol\,mL^{-1}$. A thiol-grafted magnetite nanocrystal solution (0.15 mL) was diluted to 6 mL with water and then added dropwise to the gold colloidal solution (4 mL) with vigorous stirring, producing the Au–Fe_3O_4 nanostructures.

Characterization: Morphology and size distribution of the products were characterized by using a Tecnai T12 transmission electron microscope (TEM). High-resolution TEM (HRTEM) images were obtained by using a Tecnai G2 S-Twin electron microscope operated at 200 kV. The nanocrystals dispersed in water were cast onto a carbon-coated copper grid, followed by evaporation under vacuum at room temperature.

FTIR spectra were measured in the 400–4000 cm^{-1} region by using a Bruker EQUINOX 55 spectrometer. Crystal structures were measured on a Bruker D8 Advance X-ray Diffractometer (XRD) with a $Cu_{K\alpha}$ radiation ($\lambda = 1.5418$ Å). The data were collected from $2\theta = 20$–70° at a scan rate of 0.02° per step and 1.5 s per point.

X-ray absorption spectroscopy (XAS) measurements were performed at beamline 7.0 of Advanced Light Source, Lawrence Berkeley National Laboratory. The measurements were performed at room temperature, with a base pressure in the experimental chamber lower than 5×10^{-9} mbar. XAS spectra were obtained by measuring both the total electron yield (TEY) and fluorescence yield (FY) from the sample as a function of the incoming photon energy. All spectra were normalized to the photocurrent from a clean gold mesh introduced into the beam.

The magnetic properties were measured with a magnetic properties measurement system (MPMS) from Quantum Design, which utilities a superconducting quantum interference device (SQUID) magnetometer. The magnetic moment M and the magnetic susceptibility were measured according to the following procedure: The dried nanocrystals were initially cooled in a zero field to 2 K. With an applied field of 10 Oe, the magnetization was then recorded as a ZFC curve by increasing the temperature. After the temperature had reached 350 K, the sample was progressively cooled and the magnetization was recorded as an FC curve.

Acknowledgements

Y. Yin thanks the University of California, Riverside for startup funds. M. Biasini and W. P. Beyermann were supported by the Defense Microelectronic Activity (DMEA) under agreement number DOD/DMEA H94003–06–20604. The Advanced Light Source was supported by the Director, Office of Science, Office of Basic Energy Sciences, of the U.S. Department of Energy under contract no. DE-AC02–05CH11231.

[1] H. Gu, K. Xu, C. Xu, B. Xu, *Chem. Commun.* **2006**, 941.
[2] Y. W. Jun, Y. M. Huh, J. S. Choi, J. H. Lee, H. T. Song, S. J. Kim, S. Yoon, K. S. Kim, J. S. Shin, J. S. Suh, J. Cheon, *J. Am. Chem. Soc.* **2005**, *127*, 5732.

[3] R. Weissleder, H. C. Cheng, A. Bogdanova, A. Bogdanov, *J. Magn. Reson. Imaging* **1997**, *7*, 258.
[4] F. Cengelli, D. Maysinger, F. Tschudi-Monnet, X. Montet, C. Corot, A. Petri-Fink, H. Hofmann, L. Juillerat-Jeanneret, *J. Pharmacol. Exp. Ther.* **2006**, *318*, 108.
[5] A. Petri-Fink, M. Chastellain, L. Juillerat-Jeanneret, A. Ferrari, H. Hofmann, *Biomaterials* **2005**, *26*, 2685.
[6] I. Brigger, C. Dubernet, P. Couvreur, *Adv. Drug Delivery Rev.* **2002**, *54*, 631.
[7] L. Wang, J. Bao, L. Wang, F. Zhang, Y. Li, *Chem. Eur. J.* **2006**, *12*, 6341.
[8] T. Hyeon, S. S. Lee, J. Park, Y. Chung, H. B. Na, *J. Am. Chem. Soc.* **2001**, *123*, 12798.
[9] S. Sun, H. Zeng, *J. Am. Chem. Soc.* **2002**, *124*, 8204.
[10] M. F. Casula, Y. W. Jun, D. J. Zaziski, E. M. Chan, A. Corrias, A. P. Alivisatos, *J. Am. Chem. Soc.* **2006**, *128*, 1675.
[11] A. L. Willis, N. J. Turro, S. O'Brien, *Chem. Mater.* **2005**, *17*, 5970.
[12] S. B. Wang, Y. L. Min, S. H. Yu, *J. Phys. Chem. C* **2007**, *111*, 3551.
[13] S. Si, C. Li, X. Wang, D. Yu, Q. Peng, Y. Li, *Cryst. Growth Des.* **2005**, *5*, 391.
[14] E. V. Shevchenko, D. V. Talapin, N. A. Kotov, S. O'Brien, C. B. Murray, *Nature* **2006**, *439*, 55.
[15] W. W. Yu, E. Chang, C. M. Sayes, R. Drezek, V. L. Colvin, *Nanotechnology* **2006**, *17*, 4483.
[16] J. Xie, S. Peng, N. Brower, N. Pourmand, S. X. Wang, S. Sun, *Pure Appl. Chem.* **2006**, *78*, 1003.
[17] Y. Wang, J. F. Wong, X. Teng, X. Z. Lin, H. Yang, *Nano Lett.* **2003**, *3*, 1555.
[18] R. E. Bailey, S. Nie, in *The Chemistry of Nanomaterials: Synthesis, Properties and Applications, Vol. 2* (Eds.: C. N. R. Rao, A. Müller, A. K. Cheetham), Wiley-VCH, Weinheim, **2004**, pp. 405.
[19] L. Babes, B. Denizot, G. Tanguy, J. J. Le Jeune, P. Jallet, *J. Colloid Interface Sci.* **1999**, *212*, 474.
[20] J.-R. Jeong, S.-C. Shin, S.-J. Lee, J.-D. Kim, *J. Magn. Magn. Mater.* **2005**, *286*, 5.
[21] M. P. Pileni, *J. Phys. Chem. B* **2001**, *105*, 3358.
[22] Y. Sun, Y. Xia, *Science* **2002**, *298*, 2176.
[23] H. Deng, X. L. Li, Q. Peng, X. Wang, J. P. Chen, Y. D. Li, *Angew. Chem.* **2005**, *117*, 2842; *Angew. Chem. Int. Ed.* **2005**, *44*, 2782.
[24] V. K. La Mer, R. H. Dinegar, *J. Am. Chem. Soc.* **1950**, *72*, 4847.
[25] C. B. Murray, C. R. Kagan, M. G. Bawendi, *Annu. Rev. Mater. Sci.* **2000**, *30*, 545.
[26] Y. Yin, A. P. Alivisatos, *Nature* **2005**, *437*, 664.
[27] S. A. Krasnikov, A. S. Vinogradov, K. H. Hallmeier, R. Hohne, M. Ziese, P. Esquinazi, T. Chasse, R. Szargan, *Mater. Sci. Eng. B* **2004**, *109*, 207.
[28] S. Sun, H. Zeng, D. B. Robinson, S. Raoux, P. M. Rice, S. X. Wang, G. Li, *J. Am. Chem. Soc.* **2004**, *126*, 273.
[29] D. H. Lee, R. A. Condrate, J. S. Reed, *J. Mater. Sci.* **1996**, *31*, 471.
[30] H. Li, C. P. Tripp, *Langmuir* **2005**, *21*, 2585.
[31] T. Pellegrino, L. Manna, S. Kudera, T. Liedl, D. Koktysh, A. L. Rogach, S. Keller, J. Radler, G. Natile, W. J. Parak, *Nano Lett.* **2004**, *4*, 703.
[32] G. T. Hermanson, *Bioconjugate Techniques*, Academic Press, **1996**.
[33] W. Yin, M. Chen, T. Lu, M. Akashi, X. Huang, *Eur. Polym. J.* **2006**, *42*, 1305.
[34] Y. Cui, C. Tao, Y. Tian, Q. He, J. Li, *Langmuir* **2006**, *22*, 8205.
[35] P. V. Hendriksen, S. Linderoth, P. A. Lindgård, *Phys. Rev. B* **1993**, *48*, 7259.
[36] J. P. Chen, C. M. Sorensen, K. J. Klabunde, G. C. Hadjipanayis, E. Devlin, A. Kostikas, *Phys. Rev. B* **1996**, *54*, 9288.

Received: March 6, 2007
Published online: June 15, 2007

